# Simulation of Particulate Flow Using HPC Systems


**K. Fröhlich, M. Meinke, and W. Schröder**

**Abstract** A standard strategy to predict the modulation of turbulence by the presence of particles is the two-way coupling approach, where the solid phase is approximated by point particles, which introduce sources in the momentum conservation equation. A validation of this approach is presented for isotropic decaying turbulence laden with prolate and oblate particles of Kolmogorov-length-scale size by generating highly accurate reference results via direct particle-fluid simulations, where all turbulent scales and the complete flow field in the vicinity of the particles are resolved. About 30,000 oblate and prolate particles with aspect ratios raging from 0.25 to 4 are released into the flow field. The simulation using the two-way coupled spherical and ellipsoidal Lagrangian model is compared against the reference results. The analysis of turbulent kinetic energy budgets reveals that the particles release kinetic energy into the flow field and simultaneously enhance the dissipation rate. This behavior is correctly predicted by both point-particle models. The kinetic energy of the particles, however, is significantly overestimated by the point-particle models. Moreover, the ellipsoidal Lagrangian model fails to predict the angular velocity of the particles due to the missing correlation terms for finite fluid inertia.

## 1 Introduction

Particle-laden turbulent flow is of importance in medical, natural, and technical environments such as blood flow, pollutant transport in the atmosphere and pulverized fuel combustion. A vast parameter space is introduced by the presence of the particles, which further enhances the complexity of turbulent flows. Two-way coupled Lagrangian point-particle models, where the feedback of the particles is included in the conservation equations of the flow field, have been frequently applied in direct numerical simulations (DNS) for spherical particles smaller than the Kolmogorov length $\eta_k$ in the last decades. For particle diameters $d_p > \eta_k$, however, the validity of the spherical two-way coupled Lagrangian point-particle models (SLM) is still con-

K. Fröhlich (✉) · M. Meinke · W. Schröder
Institute of Aerodynamics, RWTH Aachen University, Wüllnerstraße 5a, 52062 Aachen, Germany
e-mail: k.froehlich@aia.rwth-aachen.de



W. E. Nagel et al. (eds.), *High Performance Computing in Science and Engineering '19*,
https://doi.org/10.1007/978-3-030-66792-4_21

troversially discussed [1]. Only few studies are available on the validity of ellipsoidal Lagrangian models (ELM) for LES. While one-way coupled ELMs are frequently applied in DNS with particles smaller than $\eta_k$ [19], the accuracy of two-way coupled ELMs has not been assessed. This can be partially explained by a shortage of reference results, which can be possibly provided by fully resolved simulations. However, the resolution of thousands of Kolmogorov-length-scale size non-spherical particles requires extensive computational resources and advanced numerical algorithms.

Recently, a framework has been developed, which enables the efficient computation of sharply resolved freely moving boundaries interacting with the fluid, where the computational effort is considerably reduced by adaptive mesh refinement [13]. Subsequently, direct particle-fluid simulations (DPFS) have been generated for 45,000 spherical and ellipsoidal particles of Kolmogorov-length-scale size suspended in isotropic decaying turbulence [14], in which all particle and fluid scales are fully resolved. The identical setup has been considered in [6] with LES and DNS using SLMs, which showed a convincing accuracy for spherical particles.

In the current contribution, selected results of [5] are presented and details on computational aspects are provided. The study of [6] is extended towards non-spherical particles. Therefore, the DPFS performed in [14] will be supplemented by additional benchmark cases for oblate and prolate spheroids with varying aspect ratios. Like in [6], the quality of the point-particle models will be analyzed using DNS and LES.

## 2 Mathematical Models

### 2.1 Fluid Phase Equations

The conservation of mass, momentum, and energy in a control volume $V$ may be expressed in non-dimensional integral form by

$$\int_V \frac{\partial \boldsymbol{Q}}{\partial t}\, dV + \int_{\partial V} \bar{\boldsymbol{H}} \cdot \boldsymbol{n}\, dA = \boldsymbol{0}, \tag{1}$$

where $\boldsymbol{Q} = [\, \rho_f,\ \rho_f \boldsymbol{u}^T,\ \rho_f E \,]^T$ is the vector of conservative Eulerian variables and $\bar{\boldsymbol{H}}$ is the flux hypertensor through the surface $\partial V$ of $V$ in outward normal direction $\boldsymbol{n}$. The conservative variables are defined by the fluid density $\rho_f$, the vector of velocities $\boldsymbol{u}$, and the total specific energy $E = e + |\boldsymbol{u}|^2/2$ containing the specific internal energy $e$. The fluxes $\bar{\boldsymbol{H}}$ can be divided into an inviscid part $\bar{\boldsymbol{H}}_{inv}$ and a viscous diffusion part $\bar{\boldsymbol{H}}_{visc}$, where

$$\bar{\boldsymbol{H}} = \bar{\boldsymbol{H}}_{inv} + \bar{\boldsymbol{H}}_{visc} = \begin{pmatrix} \rho_f \boldsymbol{u} \\ \rho_f \boldsymbol{u}\boldsymbol{u} + p \\ \boldsymbol{u}\left(\rho_f E + p\right) \end{pmatrix} - \frac{1}{Re_0} \begin{pmatrix} \boldsymbol{0} \\ \bar{\boldsymbol{\tau}} \\ \bar{\boldsymbol{\tau}}\boldsymbol{u} - \boldsymbol{q} \end{pmatrix}, \tag{2}$$

with the pressure $p$, the stress tensor $\bar{\boldsymbol{\tau}}$, the vector of heat conduction $\boldsymbol{q}$, and the Reynolds number $Re_0$. The latter is determined by $Re_0 = \rho'_{f,0} a'_0 L'_0 / \mu'_0$, given the reference quantities of the density $\rho'_{f,0}$, the speed of sound $a'_0$, the dynamic viscosity $\mu'_0$, and the length $L'_0$. Using Stokes' hypothesis for a Newtonian fluid yields an equation for the stress tensor

$$\bar{\boldsymbol{\tau}} = 2\mu \bar{\boldsymbol{S}} - \frac{2}{3}\mu \left(\nabla \cdot \boldsymbol{u}\right) \bar{\boldsymbol{I}}, \tag{3}$$

in which $\bar{\boldsymbol{I}}$ is the unit tensor and $\bar{\boldsymbol{S}}$ holds the rate-of-strain tensor defined as $\bar{\boldsymbol{S}} = \left(\nabla \boldsymbol{u} + (\nabla \boldsymbol{u})^T\right)/2$. Fourier's law gives the heat conduction

$$\boldsymbol{q} = -\frac{k_T}{Pr\,(\gamma - 1)} \nabla T, \tag{4}$$

using the temperature $T$, the constant capacity ratio $\gamma = {}^{c'_{p,0}}/_{c'_{v,0}}$, and the specific heat capacities $c'_{v,0}$ and $c'_{p,0}$ at constant volume and at constant pressure. The Prandtl number $Pr$ is given by $Pr = \mu'_0 c'_{p,0} / k'_0$ containing the reference thermal conductivity $k'_0$. The dynamic viscosity $\mu$ and the thermal conductivity $k_T$ are temperature dependent and can be approximated via Sutherland's law [20]. The system of equations can be closed by the caloric state equation $e = c_v T$, and the state equation of an ideal gas $p = \rho_f R T$, with $R$ being the specific gas constant.

## 2.2 Rigid Particle Dynamics

The motion of a rigid particle can be described in the Lagrangian formulation by equations for the kinematics and dynamics, which have to be solved in point-particle models as well as in fully resolved simulations. The linear part of the kinematics in an inertial frame of reference is given by

$$\frac{d\boldsymbol{x}_p}{dt} = \boldsymbol{v}_p, \tag{5}$$

where $\boldsymbol{x}_p$ denotes the center of mass of the particle and the particle velocity $\boldsymbol{v}_p$. If the force $\boldsymbol{F}_p$ acting on the particle with mass $m_p$ is known, the dynamic relation

$$m_p \frac{d\boldsymbol{v}_p}{dt} = \boldsymbol{F}_p \tag{6}$$

closes the linear motion.

The rotational dynamics are defined in a rotating frame of reference aligned with the particle fixed coordinate system $(\tilde{x}, \tilde{y}, \tilde{z})$. The torque $\widetilde{\boldsymbol{T}}_p$ acting on the particle causes an angular acceleration with

$$\widetilde{\tilde{\boldsymbol{I}}}\frac{d\widetilde{\boldsymbol{\omega}}_{\mathrm{p}}}{dt}+\widetilde{\boldsymbol{\omega}}_{\mathrm{p}}\times\left(\widetilde{\tilde{\boldsymbol{I}}}\widetilde{\boldsymbol{\omega}}_{\mathrm{p}}\right)=\widetilde{\boldsymbol{T}}_{p}, \tag{7}$$

where $\widetilde{\tilde{\boldsymbol{I}}}$ denotes the principal moments of inertia and $\widetilde{\boldsymbol{\omega}}_p$ the angular velocity. The rotational kinematics can be described using quaternions, as described in e.g. [16].

In this contribution, volume forces such as gravity are omitted. Therefore, the coupling between the solid and the fluid frame is solely responsible for the force and the torque exerted to the particles. The coupling is established via the no-slip condition at the particle surface $\Gamma_p$

$$\boldsymbol{u}=\boldsymbol{v}_p+\boldsymbol{\omega}_p\times\left(\boldsymbol{x}_p-\boldsymbol{r}_p\right), \tag{8}$$

with $\boldsymbol{r}_p$ the local distance between the surface the center of the particle. The momentum balance given by Eq. 1 at the material interface yields the net force $\boldsymbol{F}_p$ due to fluid pressure and fluid shear forces

$$\boldsymbol{F}_p=\oint_{\Gamma_p}\left(-p\boldsymbol{n}+\bar{\boldsymbol{\tau}}\cdot\boldsymbol{n}\right)dA. \tag{9}$$

Likewise, the torque $\boldsymbol{T}_p$ acting on the particle is given by

$$\boldsymbol{T}_{\mathrm{p}}=\oint_{\Gamma_p}\left(\boldsymbol{x}-\boldsymbol{x}_p\right)\times\left(-p\boldsymbol{n}+\bar{\boldsymbol{\tau}}\cdot\boldsymbol{n}\right)dA. \tag{10}$$

The transfer of momentum at the material interface causes a direct transfer of kinetic energy into the fluid. Multiplying the momentum conservation in Eq. 1 and using Eqs. 8–10 yields the direct transfer of kinetic energy at the particle surface [14]

$$\psi_p=\oint_{\Gamma_p}\left(p\boldsymbol{n}-\bar{\boldsymbol{\tau}}\cdot\boldsymbol{n}\right)\cdot\boldsymbol{u}dA=-\left(\boldsymbol{F}_p\cdot\boldsymbol{v}_p+\boldsymbol{T}_p\cdot\boldsymbol{\omega}_p\right). \tag{11}$$

The determination of $\boldsymbol{F}_p$ and $\boldsymbol{T}_p$ as well as the coupling between the particles and the fluid in DPFS, SLMs and ELMs will be presented in the next Section.

## 3 Numerical Methods

In the following, the numerical methods for the solution of the system of equations given above will be presented. The solution scheme for Eq. 1 is based on a cell-centered finite-volume discretization on hierarchical Cartesian grids which has been described and validated in [13]. The conservative variables $\boldsymbol{Q}$ in Eq. 1 are integrated in time using an explicit five-step predictor-corrector Runge–Kutta method [13]. The

inviscid fluxes are computed by a variant of the AUSM of second-order accuracy [11]. The primitive variables at the cell surfaces are extrapolated according to the MUSCL scheme [18] using cell-centered gradients of the primitive variables obtained by a second-order least-squares approach [13]. The viscous fluxes are computed using a low-dissipation variation of the central scheme proposed in [2].

The assessment of the point-particle models in LES requires a sufficiently accurate subgrid-scale model of the turbulent flow. Based on the monotone implicit LES approach (MILES) a residual stress model has been established in [6], where mixed central and upwind stencils provide the dissipative subgrid scale contribution.

In this Section, the discretization of the equations describing the particle dynamics is introduced. First, a brief description for DPFS is provided. Subsequently, the Lagrangian two-way coupled point-particle models are described.

## *3.1 Direct Particle-Fluid Simulations (DPFS)*

Figure 1 illustrates the DPFS approach for an ellipsoidal particle of Kolmogorov-length-scale size. The Cartesian mesh is locally refined in the vicinity of the particles. More precisely, four refinement levels are introduced additionally to the DNS resolution. The geometry of the particles is analytically tracked via a level-set method developed in [8]. The interfaces of the particles are sharply resolved by reshaped Cartesian cut cells [9]. The no-slip condition is imposed on the particle surface segments and a conservative flux-redistribution technique stabilizes small cut cells [13]. The efficiency on high-performance computers is substantially improved using dynamic load balancing [12]. Isothermal conditions are considered and all cells within the solid frame can be discarded in the simulation. Due to the sharply resolved particle surface, mass, momentum, and energy are fully conserved in DPFS. The force $\boldsymbol{F}_p$ and the torque $\boldsymbol{T}_p$ can directly be obtained by summation over all discrete particle surface segments $A_i, i \in \Gamma_p$

$$\boldsymbol{F}_p = \sum_{i \in \Gamma_p} [-p\boldsymbol{n} + \bar{\boldsymbol{\tau}} \cdot \boldsymbol{n}]_i \, A_i, \tag{12}$$

$$\boldsymbol{T}_p = \sum_{i \in \Gamma_p} \big[(\boldsymbol{x} - \boldsymbol{x}_p) \times (-p\boldsymbol{n} + \bar{\boldsymbol{\tau}} \cdot \boldsymbol{n})\big]_i A_i. \tag{13}$$

Equations 5–7 are solved by the predictor-corrector scheme of second-order accuracy [13] and coupled with Eq. 1. The collision model proposed in [7] is employed to avoid overlapping bodies. The DPFS approach has been validated in [13] for several laminar and turbulent flow problems.

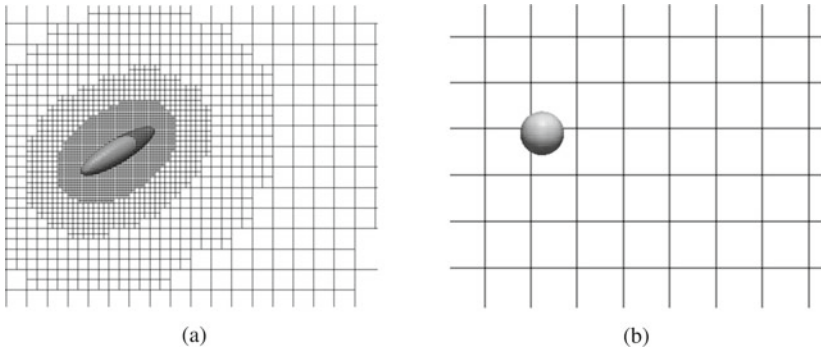


**Fig. 1** Comparison of the DPFS approach and the point-particle model: **a** A snapshot of a single ellipsoidal particle of Kolmogorov-length-scale size using DPFS. All fluid scales of the background turbulence are fully resolved with the background DNS-mesh. Four additional refinement levels are introduced to fully resolve the particle scale, i.e., particle surface, wake, and boundary layer. The particle is freely moving such that the mesh has to be adaptively refined. To establish the no-slip condition, the Cartesian cut cells are reshaped at the material interface. **b** The illustration shows a DNS mesh with the grid cell length $\Delta_{DNS}$ and the spherical Lagrangian model with the same equivalent particle diameter $d_{p,eq}$

## *3.2 Point-Particle Models*

The particle scale is not resolved in the point-particle model. To establish a feedback of the particles to the flow field, the forces and torques exerted on the particle are included in the momentum conservation in Eq. 1. A popular method is the two-way coupled point-particle model, where the force acting on the particle is projected onto the underlying grid in an actio-reactio sense similar as in, e.g., [17]. Following [6], self-induced disturbances are mostly avoided via a smooth distance-weighted feedback force. As shown in [5], the rotational contribution for turbulence modulation in isotropic turbulence is significantly smaller than the linear contribution. Therefore, the feedback of the rotational contribution of the point-particles is neglected. In this study, two different point-particle models are assessed, which will be described next.

### 3.2.1 Spherical Lagrange Model (SLM)

The SLM is not aware of the anisotropic particle shape. Hence, $\boldsymbol{F}_p$ is modeled for a sphere with the volume-equivalent particle diameter $d_{p,eq}$ neglecting the aspect ratio of the particles. That is, a simplification of the semi-empirical Maxey–Riley equation [10] for spherical particles can be used

$$\boldsymbol{F}_p = 3\pi\mu d_\mathrm{p}(\boldsymbol{u}_p - \boldsymbol{v}_p)\phi(Re_\mathrm{p}), \tag{14}$$

which represents the quasi-steady Stokes drag augmented by the Schiller-Naumann drag correlation $\phi(Re_p) = 24/Re_p(1 + 0.15Re_p^{0.687})$ with the undisturbed fluid velocity at the particle position $\boldsymbol{u}_p$. The latter has to be interpolated using the fluid velocity at the centers of the neighboring cells. To mitigate filtering errors due to interpolations, $\boldsymbol{u}_p$ is approximated by the fluid velocity at the center of the nearest cell. Although the validity of Eq. 14 is restricted to particles which are smaller than the smallest scale of the flow field $\eta_k$, it has been shown that the SLM is capable to predict the results of the DPFS for spherical particles of Kolmogorov-length scale size [6].

### 3.2.2 Ellipsoidal Lagrange Model (ELM)

The ELM considers the hydrodynamic forces and torques acting on ellipsoidal particles in creeping flow conditions. That is, the ELM is not aware of fluid inertia and therefore restricted to vanishing particle Reynolds numbers. In the ELM, the force $\boldsymbol{F}_p$ is obtained by

$$\boldsymbol{F}_p = \mu \bar{\boldsymbol{R}}^T \widetilde{\bar{\boldsymbol{K}}} \bar{\boldsymbol{R}} \left( \boldsymbol{u}_p - \boldsymbol{v}_p \right), \tag{15}$$

where $\bar{\boldsymbol{R}}$ represents a rotational matrix. The hydrodynamic torque acting on the particle is given by

$$\boldsymbol{T}_p = \mu \left( \widetilde{\bar{\boldsymbol{K}}}_s \widetilde{\boldsymbol{S}} + \widetilde{\bar{\boldsymbol{K}}}_\zeta \left( \widetilde{\boldsymbol{\zeta}} - \widetilde{\boldsymbol{\omega}}_p \right) \right), \tag{16}$$

with the fluid strain rate $\widetilde{\boldsymbol{S}}$ and $\widetilde{\boldsymbol{\zeta}}$ half times the fluid vorticity in the particle fixed coordinate system. The shape dependence of the hydrodynamic force and torque is established via the diagonal resistance matrices $\widetilde{\bar{\boldsymbol{K}}}$, $\widetilde{\bar{\boldsymbol{K}}}_s$, and $\widetilde{\bar{\boldsymbol{K}}}_\zeta$. A detailed definition of the resistance matrices is provided, e.g., in [16].

## 4 Results

The flow field of a fully periodic cube with an edge length of $L$ is initialized randomly and divergence free. The initial microscale Reynolds number is set to $Re_{\lambda 0} = u_0 \rho_f \lambda_0 / \mu = 79$, with the initial rms velocity $u_0$, the initial Taylor microscale $\lambda_0$, and $\mu$ the viscosity. The same initial flow field is used as in [14] for the DNS whereas in the case of LES, the initial energy spectrum is spectrally cut off at the highest resolvable wave number. Simulations with four resolutions are performed to assess the point-particle models. A mesh with $256^3$ cells corresponds to a DNS and meshes with $128^3$, $96^3$, and $64^3$ cells represent the LES cases. For all LES resolutions, the turbulent kinetic energy of the single phase DNS is accurately predicted, i.e., the subgrid turbulent kinetic energy is negligible. As in [6], the resolution has

**Table 1** Parameters of the particle-laden simulations at injection time $t_i^* = 0.28$: Number of particles $N_p$, aspect ratio $\beta$, density ratio particle-to-fluid $\rho_p/\rho$, ratio of the minimum particle diameter $d_{p,min}$ to the Kolmogorov length scale $\eta$, ratio of the volume-equivalent particle diameter $d_{p,eq}$ to the grid cell length of the DNS $\Delta_{DNS}$, the volume fraction $\phi_v$, and the mass fraction $\phi_m$ of the particles. Case $P2$ has been analyzed in [15]

| Case | $N_p$ | $\beta$ | $\rho_p/\rho$ | $d_{p,min}/\eta$ | $d_{p,eq}/\Delta_{DNS}$ | $d_{p,eq}/\ell$ | $\phi_v$ | $\phi_m$ |
|---|---|---|---|---|---|---|---|---|
| P2 | 45,000 | 2 | 1400 | 1.05 | 0.63 | 0.032 | $3.5 \cdot 10^{-4}$ | 0.49 |
| P4 | 25,000 | 4 | 1000 | 1.26 | 0.95 | 0.048 | $6.7 \cdot 10^{-4}$ | 0.67 |
| O4 | 20,000 | 0.25 | 1000 | 1.05 | 1.26 | 0.064 | $12.5 \cdot 10^{-4}$ | 1.25 |

**Table 2** Non-dimensional parameters of the DPFS and the single phase simulation (sP) at the time levels $t^* = 1.0$ and 2.0: Taylor-scale Reynolds number $Re_\lambda$; ratio of the volume-equivalent particle diameter $d_{p,eq}$ to the Kolmogorov length $\eta$ and the Taylor length scale $\lambda$; ratio of the particle relaxation time and the Kolmogorov time scale $\tau_p/\tau_\eta$; mean particle Reynolds number $\langle Re_p \rangle$

| Case | $t^* = 1.0$ | | | | | $t^* = 2.0$ | | | | |
|---|---|---|---|---|---|---|---|---|---|---|
| | $Re_\lambda$ | $d_{p,eq}/\eta$ | $d_{p,eq}/\lambda$ | $\tau_p/\tau_\eta$ | $\langle Re_p \rangle$ | $Re_\lambda$ | $d_{p,eq}/\eta$ | $d_{p,eq}/\lambda$ | $\tau_p/\tau_\eta$ | $\langle Re_p \rangle$ |
| sP | 36.6 | – | – | – | – | 31.8 | – | – | – | – |
| P2 | 26.3 | 1.12 | 0.11 | 97.9 | 6.6 | 17.8 | 0.84 | 0.10 | 56.9 | 4.5 |
| P4 | 24.7 | 1.73 | 0.18 | 167.6 | 10.1 | 15.6 | 1.32 | 0.17 | 98.0 | 7.25 |
| O4 | 24.9 | 2.49 | 0.25 | 346.9 | 14.0 | 14.7 | 2.04 | 0.27 | 232.4 | 11.2 |

only minor impact on the statistics. Therefore, only the results of the LES cases with $64^3$ cells are presented.

Three particle-laden cases are considered. The particles are introduced at the insertion time $t_i^* = 0.28$, where $t^* = t\epsilon_0/u_0^2$ is normalized by the initial eddy turnover time using the initial viscous dissipation rate $\epsilon_0$. As in [14], the particles are initialized with the local fluid velocity and zero angular velocity. Table 1 lists the non-dimensional parameters related to the particles and Table 2 specifies non-dimensional parameters for $t^* = 1.0$ and 2.0. The prolate case $P2$ considered in [15] is supplemented by case $P4$ for prolate spheroids with an aspect ratio of $\beta = 4$ and by case $O4$ for oblate spheroids with an aspect ratio of $\beta = 0.25$. All particle-laden flows are dilute and assigned to the two-way coupling regime [3]. The single phase DNS will be denoted case $sP$.

## *4.1 Direct Particle-Fluid Simulation (DPFS)*

Next, budgets of the turbulent kinetic energy defined by $E_\mathrm{k} = \langle \rho \boldsymbol{u'}^2/2 \rangle$, where the brackets $\langle\ \rangle$ denote the spatial ensemble average and $\boldsymbol{u'}$ the rms-velocity vector, are considered. For DPFS, the budget reads [14]

$$\frac{\partial E_k}{\partial t}(t) = \Psi(t) - \mathcal{E}(t) \tag{17}$$

where the total kinetic energy transfer $\Psi(t)$ on the particle surfaces can be computed by Eq. 11, i.e.,

$$\Psi(t) = \sum_{p=1}^{N_p} \psi_p = -\sum_{p=1}^{N_p} \left( \boldsymbol{F}_p \cdot \boldsymbol{v}_p + \boldsymbol{T}_p \cdot \boldsymbol{\omega}_p \right). \tag{18}$$

The integral viscous dissipation rate $\mathcal{E}(t)$ of incompressible flows can be determined by integrating the local dissipation rate $\epsilon$ over the fluid domain $V_f$, i.e.,

$$\mathcal{E}(t) = \int_{V_f} \epsilon dV = \int_{V_f} 2\mu \bar{\boldsymbol{S}} : \bar{\boldsymbol{S}} dV, \tag{19}$$

where $\bar{\boldsymbol{S}} : \bar{\boldsymbol{S}}$ denotes the inner product of the strain-rate tensor. It has been shown in [14], that the viscous dissipation rate can be decomposed in a background dissipation rate $\overline{\mathcal{E}}$ and a particle-induced dissipation rate $\mathcal{E}_p$ in the vicinity of the particles with

$$\mathcal{E}(t) = \overline{\mathcal{E}}(t) + \mathcal{E}_p(t) = \overline{\mathcal{E}}(t) + \sum_{p=1}^{N_p} \boldsymbol{F}_p \cdot \left( \boldsymbol{U}_p - \boldsymbol{v}_p \right) + \boldsymbol{T}_p \cdot \left( \boldsymbol{\Omega}_p - \boldsymbol{\omega}_p \right) + \mathcal{I}_f, \tag{20}$$

where $\boldsymbol{U}_p - \boldsymbol{v}_p$ represents the relative velocity vector and $\boldsymbol{\Omega}_p - \boldsymbol{\omega}_p$ the relative angular velocity vector of a particle and the surrounding fluid. The term $\mathcal{I}_f$ represents the contribution of the fluid inertia in the vicinity of the particles. The particle-induced dissipation $\mathcal{E}_p$ is an analytical expression, which has been derived using the momentum conservation equation in Eq. 1. The term $\boldsymbol{U}_p$ represents the ambient fluid velocity seen by the particles and is approximated as in [14].

Likewise, the global kinetic energy of the particles $K(t) = \sum(m\boldsymbol{v}_p^2 + \widetilde{\boldsymbol{\omega}} \cdot (\widetilde{\boldsymbol{I}}\widetilde{\boldsymbol{\omega}}))/2$ is described by

$$\frac{dK}{dt} = -\Psi(t). \tag{21}$$

In the following, the different contributions of the turbulent kinetic energy budget generated via DPFS are presented. The contributions in Eq. 17 are normalized by the reference dissipation $\epsilon_{ref} = \rho u_0^3 / L$ and the turbulent kinetic energy is normalized by its initial value $E_{k,0}$. Figure 2a shows the temporal development of the turbulent kinetic energy $E_k$. Moderate attenuation is observed in comparison to the single-phase DNS. Despite the substantially different setups of the particles for all cases, the modulation of the turbulent kinetic energy is very similar. Figure 2b shows the mean rate of total kinetic energy transfer $\langle \psi_p \rangle(t) = \Psi(t)/V_f$. All cases indicate a source of turbulent kinetic energy after an initial build-up. The case $O4$ is substantially larger than the cases $P2$ and $P4$. Figure 2c shows the mean viscous dissipation rate $\langle \epsilon \rangle(t) = \mathcal{E}(t)/V_f$. At insertion time, the viscous dissipation rate shows a sharp peak

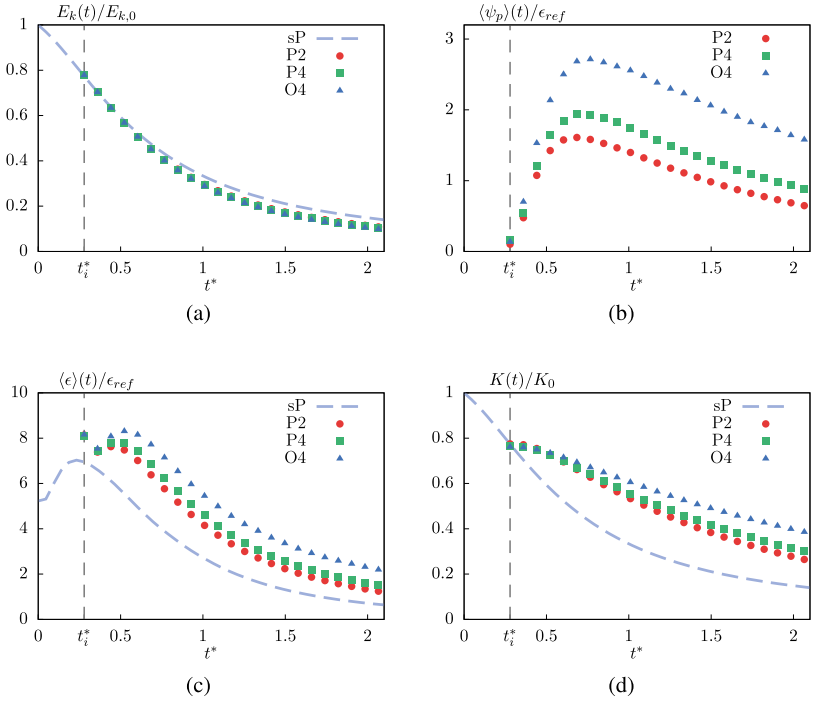


**Fig. 2** Direct particle-fluid simulation of isotropic decaying turbulence laden with prolate ellipsoids with an aspect ratio of $\beta = 2$ ($P2$) and $\beta = 4$ ($P4$), and oblate particles ($O4$). The single phase results are shown as a reference (sP-DNS). Nondimensional temporal development of: **a** turbulent kinetic energy $E_k(t)$ normalized by its initial value $E_{k,0}$; **b** mean rate of total kinetic energy transfer $\langle\psi\rangle(t) = \Psi(t)/V_f$ normalized by the reference dissipation $\epsilon_{ref} = \rho u_0^3/L$; **c** mean viscous dissipation rate $\langle\epsilon\rangle(t) = \mathcal{E}(t)/V_f$ normalized by the reference dissipation $\epsilon_{ref}$; and **d** total kinetic energy of the particles $K(t)$ normalized by $K_0 = \phi_m E_{k,0}$

due to the instantaneous build-up of the boundary layers. Similarly to the transfer of kinetic energy, the case $O4$ shows a larger dissipation rate. This explains the almost identical development of the turbulent kinetic energy for the three cases. The additional transfer of kinetic energy correlates with a higher viscous dissipation rate. The total kinetic energy of the particles $K(t)$ normalized by $K_0 = \phi_m E_{k,0}$ is presented in Fig. 2d. In all cases, the turbulent kinetic energy decays substantially faster than the kinetic energy of the particles. At insertion time, the particles have the same velocity as the surrounding fluid such that the total kinetic energy transfer vanishes. Immediately after insertion, the particles leave their initial position. The larger particles in case $P4$ and $O4$ maintain their kinetic energy for a longer time, which leads to a higher velocity difference vector and therefore a higher viscous dissipation rate and transfer of kinetic energy.

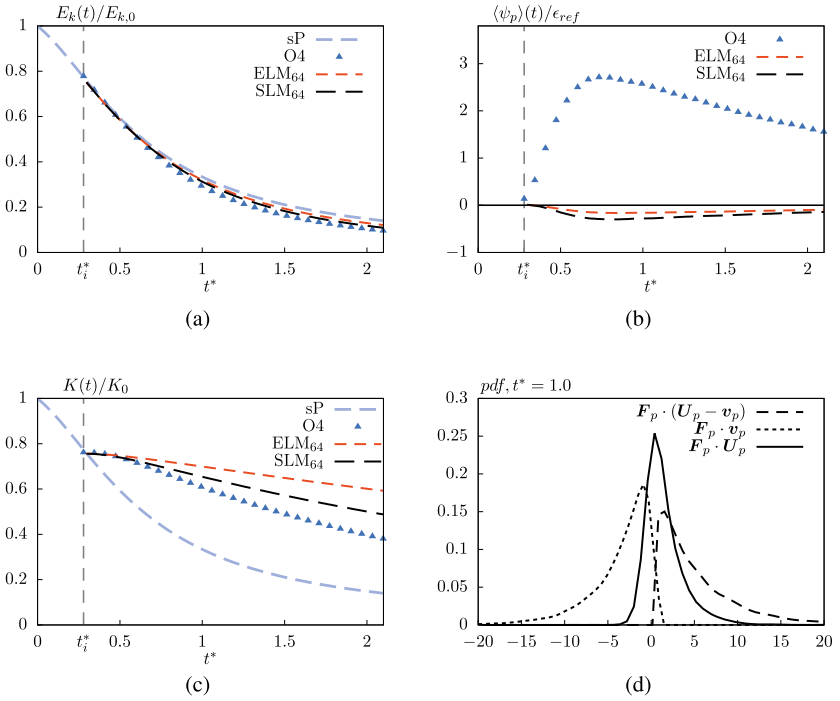


**Fig. 3** Comparison of the LES using the spherical Langrangian model $SLM_{64}$ and the ellipsoidal Langrangian model $ELM_{64}$ against the reference results of DPFS for oblate particles ($O4$). The single phase results are shown as a reference (sP). Nondimensional temporal development of: **a** turbulent kinetic energy $E_k(t)$ normalized by its initial value $E_{k,0}$; **b** mean rate of total kinetic energy transfer $\langle\psi\rangle(t) = \Psi(t)/V_f$ normalized by the reference dissipation $\epsilon_{ref} = \rho u_0^3/L$; **c** total kinetic energy of the particles $K(t)$ normalized by $K_0 = \phi_m E_{k,0}$; **d** shows the probability density function (pdf) of the particle-induced contributions by the linear dynamics in the turbulent kinetic energy budgets normalized by the reference dissipation $\epsilon_{ref}$. The probability density function (pdf) is generated using $SLM_{64}$ for case $O4$ at $t^* = 1.0$ and the pdf values are normalized by $u^3 d_p^2$. The dashed line represents the particle-induced dissipation rate, the dotted line is the direct transfer of kinetic energy, and the full line the total contribution of the particles in the budget

## 4.2 Assessment of LES Using Point-Particle Models

In this Section, the LES using an SLM ($SLM_{64}$) and an ELM ($ELM_{64}$) are validated against the reference results of the DPFS. Four different resolutions have been simulated for this study, where the mesh size ranges from $64^3$ cells to $256^3$ cells corresponding to a DNS. The statistics, which are presented hereafter, show only minor differences between the resolutions. Therefore, only the results of an LES with $64^3$ cells are shown. For instance, case $O4$ will be presented in detail whereas the other cases are only outlined, if the results are significantly different.

Figure 3a shows the temporal development of the turbulent kinetic energy predicted by $SLM_{64}$ and $ELM_{64}$ compared to the DPFS. Consistently with the DPFS,

the point-particle models predict a moderate attenuation. The $\mathrm{ELM}_{64}$ slightly overestimates the turbulent kinetic energy, while the $\mathrm{SLM}_{64}$ is close to the DPFS. For point-particle models, the budget Eq. 17 reads [4]

$$\frac{\partial E_k}{\partial t}(t) = -\overline{\mathcal{E}}(t) - \boldsymbol{F}_p \cdot \boldsymbol{U}_p. \tag{22}$$

The point-particle model implicitly combines the particle-induced dissipation $\mathcal{E}_p$ with the direct transfer of kinetic energy $\Psi(t)$ [6, 14] neglecting the fluid inertia term $\mathcal{I}_f$. For the subsequent comparison, the mean rate of the turbulent kinetic energy transfer $\langle\psi_p\rangle(t)$ is redefined for point-particle models with $\langle\psi_p\rangle(t) = -\frac{1}{V_f}\sum_{p=1}^{N_p} \boldsymbol{F}_p \cdot \boldsymbol{U}_p$ to be consistent with other studies using two-way coupled point-particle models (e.g. [4]).

Figure 3b depicts the kinetic energy transfer of the point-particle models compared to the DPFS. Both models predict a sink of turbulent kinetic energy, which corresponds to the attenuated energy shown in Fig. 3a. Due to the different definitions of the kinetic energy transfer, the differences between the reference results of the DPFS and the point-particle models are substantial. The total kinetic energy of the particles $K(t)$ is shown in Fig. 3c. The point-particle models significantly overestimate the kinetic energy of the particles. Based on the reference results of the DPFS, the kinetic energy is 12.6% higher in the $\mathrm{SLM}_{64}$ and 24.8% higher in $\mathrm{ELM}_{64}$ at $t^* = 1.5$. The $\mathrm{SLM}_{64}$ is not aware of the anisotropy of the particles and uses empirical drag correlations for finite fluid inertia, which is valid for spherical particles. This leads to an underestimation of the forces acting on the particles and the initial kinetic energy of the particles remains longer during the decay of the turbulence. The $\mathrm{ELM}_{64}$ fails to predict the DPFS results. At this particle Reynolds number, the fluid inertia has to be taken into account to predict the linear dynamics of the particles. Figure 3d depicts the pdf of the linear contribution of the particles in the turbulent kinetic energy budget generated using $\mathrm{SLM}_{64}$. The model predicts that the direct transfer of kinetic energy $\boldsymbol{F}_p \cdot \boldsymbol{v}_p$ is a source in the budget, which is largely eliminated by the particle-induced dissipation $\boldsymbol{F}_p \cdot \left(\boldsymbol{U}_p - \boldsymbol{v}_p\right)$. Note that both contributions are not resolved in the simulations using point-particle models but only recovered indirectly for the statistics. That is, the force is modeled via Eq. 14 and $\boldsymbol{U}_p$ is the velocity of the cell containing the point particle. The total contribution $\boldsymbol{F}_p \cdot \boldsymbol{U}_p$ is, however, different from the reference of DPFS. It can be expected that the differences are significantly larger for setups, in which the direct transfer of kinetic energy is not balanced by the particle-induced dissipation.

Figure 4a shows a comparison of the value of the particle angular velocity $|\boldsymbol{\omega}_p|$. The data of the $\mathrm{ELM}_{64}$ are compared against the DPFS. Since these statistics depend on the resolution of the background flow, the data of a DNS using the ELM ($\mathrm{ELM}_{256}$) are included in the figure. A broad distribution of the angular velocity can be observed for the case $O_4$. The ELM fails to predict this distribution and shows a sharp peak at low angular velocities for both resolutions. The case $P_4$ is presented in Fig. 4b. The DPFS shows a narrower distribution than for case $O_4$, whereas the ELM predicts a wider distribution. The prediction of the ELM is better than for the case $O4$,

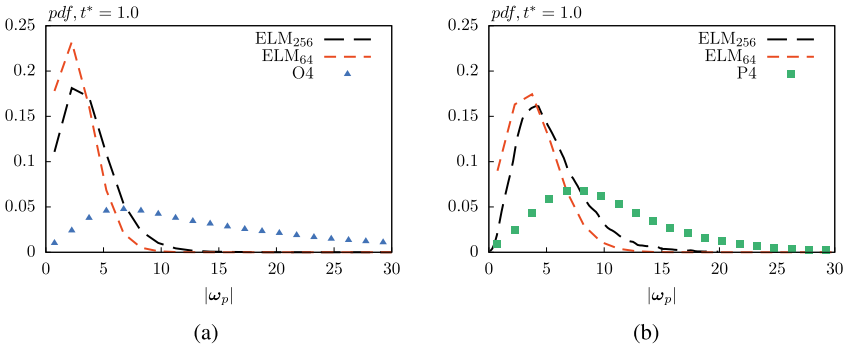


**Fig. 4** Comparison of the results using the ellipsoidal Langrangian model ELM against the reference results of DPFS. A DNS using the ELM corresponds to ELM$_{256}$ and the LES corresponds to ELM$_{64}$. The figures show the absolute value of the angular velocities of the particles $|\boldsymbol{\omega}_p|$ normalized by $u_0/L$ for ellipsoidal particles with aspect ratio of **a** $\beta = 0.25$ and **b** $\beta = 4$

but still shows significant deviations. Again a dependence on the resolution of the turbulence can be observed. As for the linear dynamics, the rotational dynamics are not accurately predicted, which can be explained by missing correlations for the fluid inertia in the formulation of the ELM.

## 5 Conclusion

The accuracy of LES using two-way coupled ellipsoidal and spherical Lagrangian models in isotropic decaying turbulence is analyzed. Reference results are generated via direct particle-fluid simulation, where an adaptively refined Cartesian cut-cell mesh is employed to completely resolve all fluid and particle scales. A dilute suspension laden with particles of Kolmogorov-length-scale size is considered, where turbulence modulation may appear but collisions are not statistically important, i.e., a two-way coupled suspension. The particle aspect ratio ranges from $\beta = 0.25$ to 4. Turbulent kinetic energy budgets are presented. The particles transfer kinetic energy into the flow field, which is mainly dissipated in the boundary layers and wakes of the particles. Moderate turbulence attenuation is observed in comparison to the single phase flow. This behavior is accurately predicted by the LES using point-particle models. The particle dynamics, however, are not accurately predicted by the Lagrangian models. The ellipsoidal model significantly overestimates the kinetic energy of the particles during the decay process, because it assumes a vanishing particle Reynolds number, i.e., it neglects the fluid inertia. The spherical Lagrangian model takes the fluid inertia into account but neglects the anisotropic particle shape. Although the results are closer to the reference, the spherical Lagrangian model still overestimates the kinetic energy of the particles. These observations hold for all resolutions of the LES, where the turbulent kinetic energy is not filtered significantly.

If an orientation dependent correlation for finite fluid inertia is used, the rotational dynamics define the orientation and thus, the linear dynamics of the particles. The rotation is, however, not correctly predicted by the ellipsoidal model. A full set of correlation terms for linear and rotational dynamics might be required, although the linear velocity difference between particles and surrounding fluid almost completely defines the turbulence modulation.

## 6 Computational Resources

The DPFS performed in this contribution contains up to 45,000 fully resolved particles to provide a sufficiently large number of samples for converged particle statistics. The parameter setup is chosen to study the effects of the particle shape on turbulence modulation and particle dynamics. A minimum resolution of 10 cells per particle diameter is required in the vicinity of each particle to provide sufficient accuracy of the near-particle hydrodynamics. In total, approx. 2 billion cells are required to resolve the near-particle flow field. Each of the simulation is performed on 2000 nodes using about 40 TB of RAM distributed over 48,000 CPU cores. Dynamic load balancing is applied using an automatic redistribution of the cells on a weighted Hilbert curve [12]. The post-processing of the results require the whole instantaneous flow field for a statistically sufficient amount of time steps. Therefore, the large amount of data has to be partially analyzed in-Situ, since the computation lasts $\mathcal{O}(10^5) - \mathcal{O}(10^6)$ time steps, where each time step would require 270 GB disk space.

**Acknowledgements** This work has been financed by the German Research Foundation (DFG) within the framework of the SFB/Transregio 'Oxyflame' (subproject B2). The support is gratefully acknowledged. Computing resources were provided by the High Performance Computing Center Stuttgart (HLRS) and by the Jülich Supercomputing Center (JSC) within a Large-Scale Project of the Gauss Center for Supercomputing (GCS).

## References

1. S. Balachandar, J.K. Eaton, Turbulent dispersed multiphase flow. Annu. Rev. Fluid Mech. **42**, 111–133 (2010)
2. M. Berger, M. Aftosmis, Progress towards a Cartesian cut-cell method for viscous compressible flow, in *AIAA Paper 2012–1301* (2012)
3. S. Elghobashi, On predicting particle-laden turbulent flows. Appl. Sci. Res. **52**(4), 309–329 (1994)
4. A. Ferrante, S. Elghobashi, On the physical mechanisms of two-way coupling in particle-laden isotropic turbulence. Phys. Fluids **15**(2), 315–329 (2003)
5. K. Fröhlich, L. Schneiders, M. Meinke, W. Schröder, Assessment of non-spherical point-particle models in LES using direct particle-fluid simulations, in *AIAA Paper 2018–3714* (2018)
6. K. Fröhlich, L. Schneiders, M. Meinke, W. Schröder, Validation of Lagrangian two-way coupled point-particle models in large-Eddy simulations. Flow Turbul. Combust. **101**(2), 317–341 (2018)

7. R. Glowinski, T. Pan, T. Hesla, D. Joseph, J. Periaux, A fictitious domain approach to the direct numerical simulation of incompressible viscous flow past moving rigid bodies: application to particulate flow. J. Comput. Phys. **169**(2), 363–426 (2001)
8. C. Günther, M. Meinke, W. Schröder, A flexible level-set approach for tracking multiple interacting interfaces in embedded boundary methods. Comput. Fluids **102**, 182–202 (2014)
9. D. Hartmann, M. Meinke, W. Schröder, A strictly conservative Cartesian cut-cell method for compressible viscous flows on adaptive grids. Comput. Meth. Appl. Mech. Eng. **200**(9), 1038–1052 (2011)
10. M.R. Maxey, J.J. Riley, Equation of motion for a small rigid sphere in a nonuniform flow. Phys. Fluids **26**(4), 883–889 (1983)
11. M. Meinke, W. Schröder, E. Krause, T. Rister, A comparison of second-and sixth-order methods for large-Eddy simulations. Comput. Fluids **31**(4), 695–718 (2002)
12. L. Schneiders, J.H. Grimmen, M. Meinke, W. Schröder, An efficient numerical method for fully-resolved particle simulations on high-performance computers. PAMM **15**(1), 495–496 (2015)
13. L. Schneiders, C. Günther, M. Meinke, W. Schröder, An efficient conservative cut-cell method for rigid bodies interacting with viscous compressible flows. J. Comput. Phys. **311**, 62–86 (2016)
14. L. Schneiders, M. Meinke, W. Schröder, Direct particle-fluid simulation of Kolmogorov-length-scale size particles in decaying isotropic turbulence. J. Fluid Mech. **819**, 188–227 (2017)
15. L. Schneiders, M. Meinke, W. Schröder, On the accuracy of Lagrangian point-mass models for heavy non-spherical particles in isotropic turbulence. Fuel **201**, 2–14 (2017)
16. C. Siewert, R. Kunnen, M. Meinke, W. Schröder, Orientation statistics and settling velocity of ellipsoids in decaying turbulence. Atmos. Res. **142**, 45–56 (2014)
17. K.D. Squires, J.K. Eaton, Particle response and turbulence modification in isotropic turbulence. Phys. Fluids A **2**(7), 1191–1203 (1990)
18. B. van Leer, Towards the ultimate conservative difference scheme. V. A second-order sequel to Godunov's method. J. Comput. Phys. **32**(1), 101–136 (1979)
19. G.A. Voth, A. Soldati, Anisotropic particles in turbulence. Annu. Rev. Fluid Mech. **49**, 249–276 (2017)
20. F.M. White, *Viscous Fluid Flow* (McGraw-Hill, 1991)